The Effect of CWTSAW on the Toughness of Heavy-Gauge X70: Part I – Correlating HAZ Microstructure with Cold Wire Feed Rate

The effects of cold wire feed rate on martensite-austenite constituent morphology and prior austenite grain size of cold-wire tandem submerged-arc welded X70 steel were studied

BY T. REN, J. B. WISKEL, G. LEHNHOFF, D. G. IVEY, L. LI, L. COLLINS, M. GAUDET, E. WILLETT, AND H. HENEIN

Abstract

The effect of cold wire feed rate (CWFR) on martensite-austenite (MA) constituent morphology and prior austenite grain (PAG) size in the heat-affected zone (HAZ) of heavy gauge (19.1 mm thick) X70 microalloyed steel welded by cold-wire tandem submerged-arc welding (CWTSAW) was studied. A series of single-pass CWTSAW trials were made using cold wire feed rates (CWFRs) of 0 mm/s, 16.9 mm/s, and 33.9 mm/s, which corresponded to effective heat inputs of 2.9 kJ/mm, 2.6 kJ/mm, and 2.3 kJ/mm, respectively. The PAG size and MA constituent morphology (area and aspect ratio distribution) were measured using optical microscopy. The average PAG size in the coarse-grained HAZ (CGHAZ) was reduced from 139 μm to 83 μm as the CWFR was increased from 0 mm/s (2.9 kJ/mm) to 33.9 mm/s (2.3 kJ/mm). The total number of MA constituents and the area fraction of MA in the CGHAZ were lowest for the intermediate CWFR of 16.9 mm/s (2.6 kJ/mm).

Keywords

- Cold-Wire Tandem Submerged-Arc Welding
- Martensite-Austenite Morphology
- Prior Austenite Grains
- Charpy Toughness
- Micro-Hardness

Introduction

For heavy gauge microalloyed steel line pipe (> 17 mm), tandem submerged-arc welding (TSAW) is used to produce line pipe sections due to its deeper penetration, improved deposition rate, and greater productivity compared with conventional submerged-arc welding (Ref. 1). However, using tandem electrodes can lead to excessive heat input, adversely impacting the toughness of the coarse-grained heat-affected zone (CGHAZ). To reduce the effective heat input (i.e., maintain and/or improve CGHAZ toughness), cold-wire TSAW (CWTSAW) has been developed (Ref. 2).

CWTSAW is a welding process consisting of three electrodes, including a lead electrode, a trail electrode, and a cold electrode (no current is applied to this wire). Cold-wire in conventional submerged-arc welding has been applied to an X65 plate (Ref. 3). A cold wire feed rate (CWFR) of 38.1 mm/s in the root pass and of 46.6 mm/s in the fill/cap pass increased the deposition rate by 32% and 39%, respectively (Ref. 3). The weld centerline Charpy toughness was maintained. CWTSAW has also been applied to an intermediate gauge (13.4 mm) X70 plate (Refs. 4, 5). A CWFR of 4.2 mm/s increased the heat-affected zone (HAZ) Charpy impact energy to –45°C by 38% compared with the conventional TSAW process. The enhanced absorbed energy was attributed to a finer prior austenite grain (PAG) size (reduced from 69 μm to 55 μm) and a reduced area fraction of martensite-austenite (MA) constituents.

Toughness in the HAZ of microalloyed steels, particularly the CGHAZ, can decrease significantly due to the presence of local brittle zones consisting of coarsened PAGs and MA constituents, which are closely related to welding heat input (Refs. 5–8). MA constituents that form at PAG boundaries and/or within the interior of PAGs consist of untempered martensite and retained austenite in both X70 and X80 line

https://doi.org/10.29391/2025.104.008

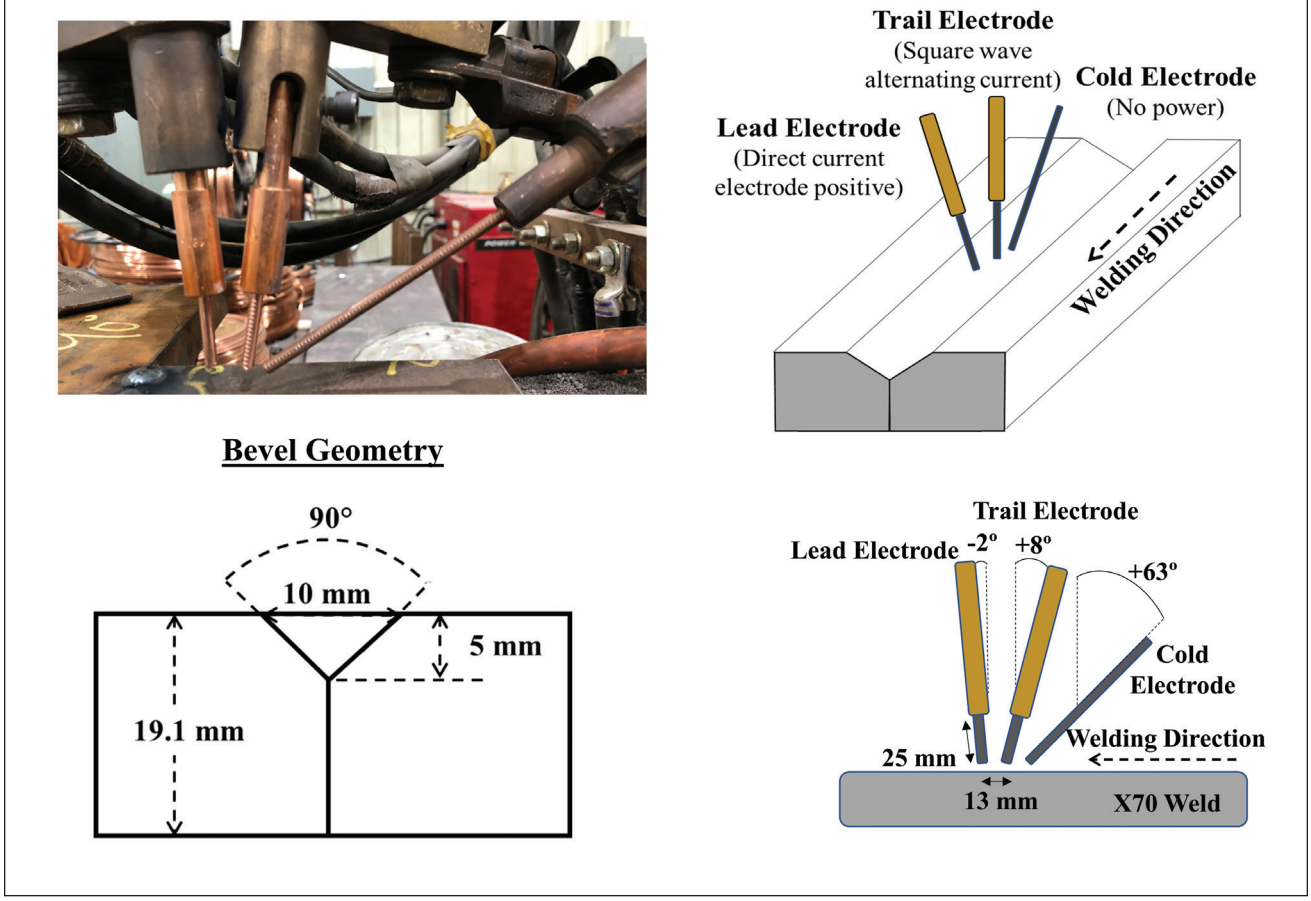

Fig. 1 — Cold-wire tandem submerged-arc welding (CWTSAW) test weld configuration.

pipe steels (Refs. 9, 10). Charpy impact energies measured from Gleeble-simulated CGHAZ regions for X70 pipeline steel have been shown to be dependent on the PAG size and MA morphology, such as area fraction and MA size (Refs. 11–13). The average PAG size and MA size have been correlated with welding thermal cycles applied through Gleeble testing, particularly the time duration above A_{c1} and the rate of cooling. For a holding temperature of 850°C, the average MA size changed from 3.5 µm to 2.9 µm as the rate of cooling was increased from 2°C/s to 10°C/s (Ref. 14). At a constant cooling rate of 15°C/s, the PAG size increased from 17 µm to 68 µm as the holding temperature was increased from 1100°C to 1300°C for durations above A_{c1} (Ref. 15). In addition, the average MA size was not altered by changes in the PAG size alone but by the variation in PAG size (PAG boundaries are nucleation sites for ferrite) and rate of cooling (high rates can lead to displacive martensite transformation) (Refs. 14, 15). In this study, the time duration above A_{c1} and the rate of cooling in the CGHAZ were simultaneously altered by the fusion of the cold wire addition in the molten pool. In previous work (Ref. 2) by the authors on heavy gauge (19.1 mm thick) X70 steel, increased CWFR levels were found to decrease PAG size and alter the MA morphology in the CGHAZ. However, only a limited quantitative correlation between MA morphology and PAG size distributions in the CGHAZ of heavy gauge welds by CWTSAW with different CWFR levels has been done.

The work presented in this article (Part I) aims to establish the quantitative distribution of MA morphology and PAG size altered by the CWFR in the CGHAZ of heavy gauge (19.1 mm thick) X70 CWTSAW welds. A series of CWTSAW trials were conducted on heavy gauge (19.1 mm thick) X70 steel using three levels of CWFR, including 0 mm/s, 16.9 mm/s, and 33.9 mm/s, which are equivalent to effective heat inputs of 2.9 kJ/mm, 2.6 kJ/mm, and 2.3 kJ/mm, respectively. The area and aspect ratio distribution of each MA constituent in the CGHAZ/fine-grained HAZ (FGHAZ) and the size of the PAGs in the CGHAZ were measured at the quarter thickness using image processing software (MATLAB R2022b and ImageJ) applied to optical microscopy (OM) images. The microscopic features of PAGs and MA constituents in the CGHAZ were characterized by scanning electron microscopy (SEM). The effects of effective heat input on the measured MA morphology and PAG size distribution are discussed. Part II of this paper will correlate the measured MA morphology and PAG size distributions with Charpy impact energy, notch position, and fracture length.

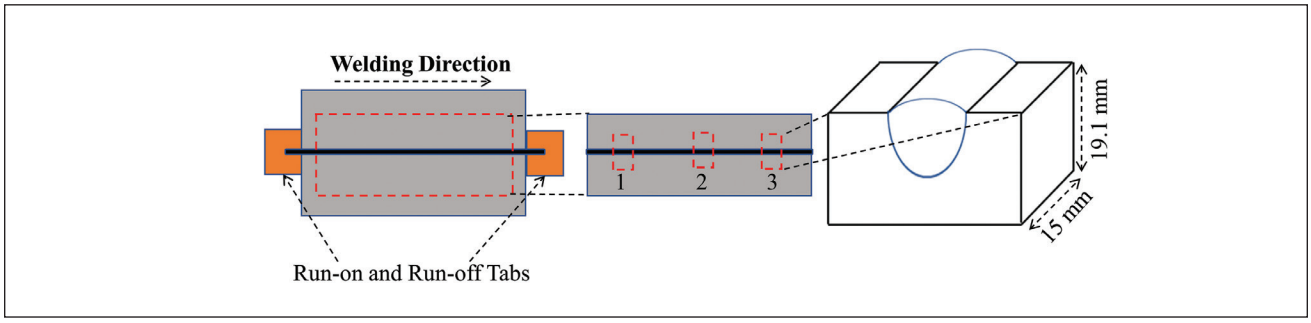

Fig. 2 — Schematic showing the extraction of test samples.

Table 1 — Composition of X70 and S2Mo Bare Electrode (wt-%)

X70	C	Mn	Si	N	V + Mo + Ti + Nb	Cu + Ni + Cr	P_{cm}
	0.04	1.29	0.28	0.006	0.34	0.63	0.16
Bare Electrode	C	Mn	Si	Mo	Ni	Cr	Cu
	0.1	1.04	0.1	0.56	0.02	0.03	0.03

Table 2 — CWTSAW Test Weld Parameters

Welding Parameters		Welding Trials		
	Unit	2.9 kJ/mm	2.6 kJ/mm	2.3 kJ/mm
Heat Input — Lead	kJ/mm	1.6	1.6	1.6
Heat Input — Trail	kJ/mm	1.3	1.3	1.3
Voltage — Lead	V	31	31	31
Voltage — Trail	V	33.5	33.5	33.5
Current — Lead	A	1100	1100	1100
Current — Trail	A	825	825	825
Travel Speed	mm/s	21.2	21.2	21.2
Cold Wire Feed Rate	mm/s	0	16.9	33.9
Effective Heat Input (Ref. 19)	kJ/mm	2.9	2.6	2.3

Experimental Procedure

Materials and Welding Procedure

The compositions of the X70 steel plate and the bare electrodes (lead, trail, and cold electrodes) studied are shown in Table 1. The heavy gauge (19.1 mm thick) X70 steel was produced by thermo-mechanically controlled processing (Ref. 1). The weld crack susceptibility index (P_{cm}) for X70 steel is 0.16 wt-%. To put this value in context, steel with a P_{cm} value of 0.35 wt-% or lower is considered to have good weldability (Ref. 16). The 4.0 mm S2Mo electrodes and cold wires were selected according to AWS A5.23, *Specification*

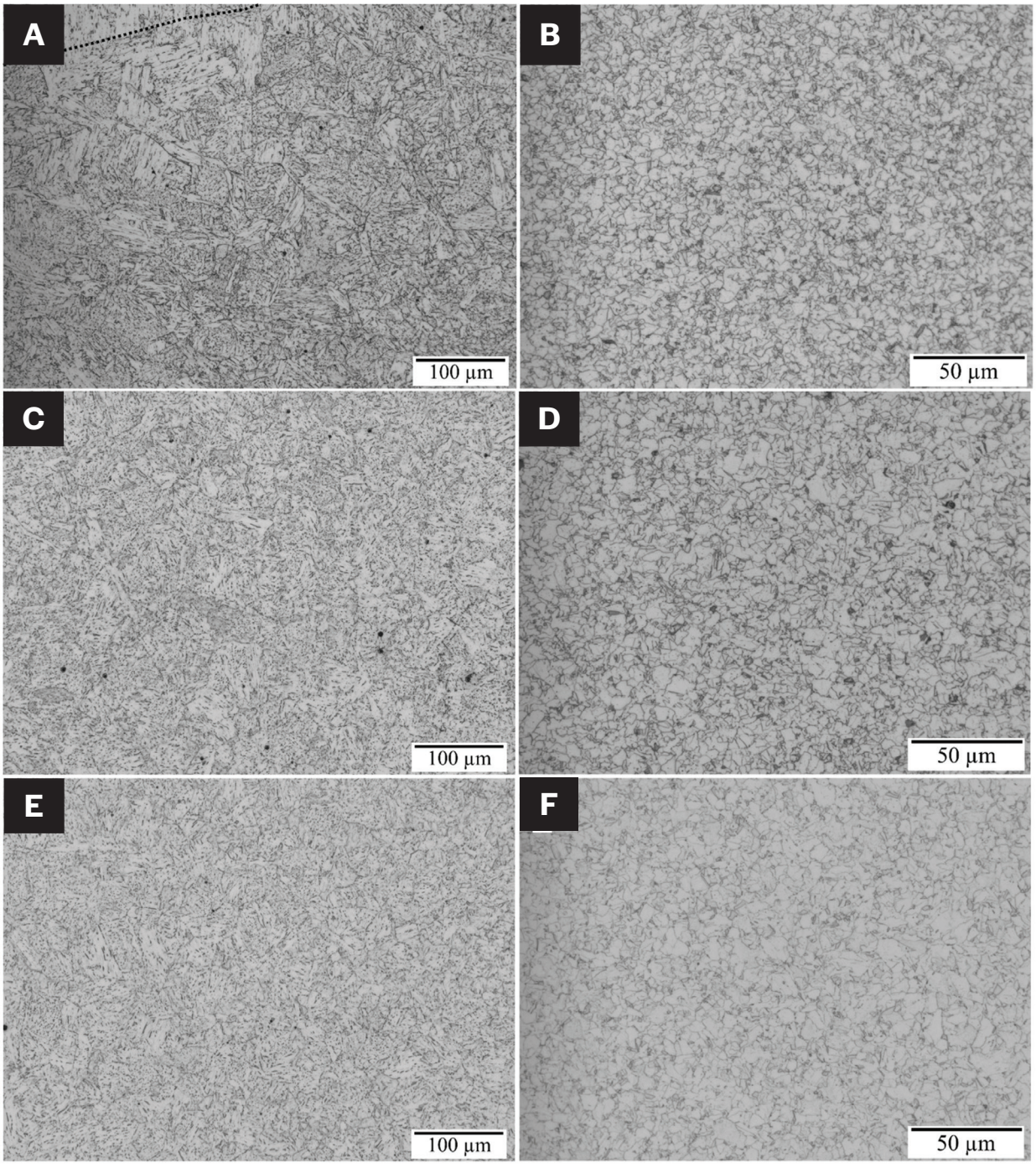

Fig. 3 — Optical micrographs of nital etched microstructures in the CGHAZ (A, C, E) and FGHAZ (B, D, F): A, B — 2.9 kJ/mm; C, D — 2.6 kJ/mm; E, F — 2.3 kJ/mm.

for Low-Alloy and High Maganese Steel Electrodes and Fluxes for Submerged Arc Welding (Ref. 17).

The CWTSAW process included lead, trail, and cold electrodes, as shown in Fig. 1. Direct current electrode positive and alternating current square wave modes were selected for the lead and trail electrodes, respectively. The current was not applied to the cold electrode. The angular positions for each electrode were –2, 8, and 63 deg for the lead, trail, and cold wires, respectively. The combination of direct and alternating current was used to achieve a deep penetration profile and a high deposition rate (Ref. 18). A BF6.5 consumable flux (EN 760) was used in the CWTSAW process. Weld coupons were fabricated with the bevel specifications shown in Fig. 1.

The welding parameters for the test welds are shown in Table 2 and include the voltage (V), current (I), and calculated heat input (HI) for both the lead and trail electrodes. The lead and trail electrodes' nominal heat input ($HI_{Nominal}$) were calculated according to Equation 1.

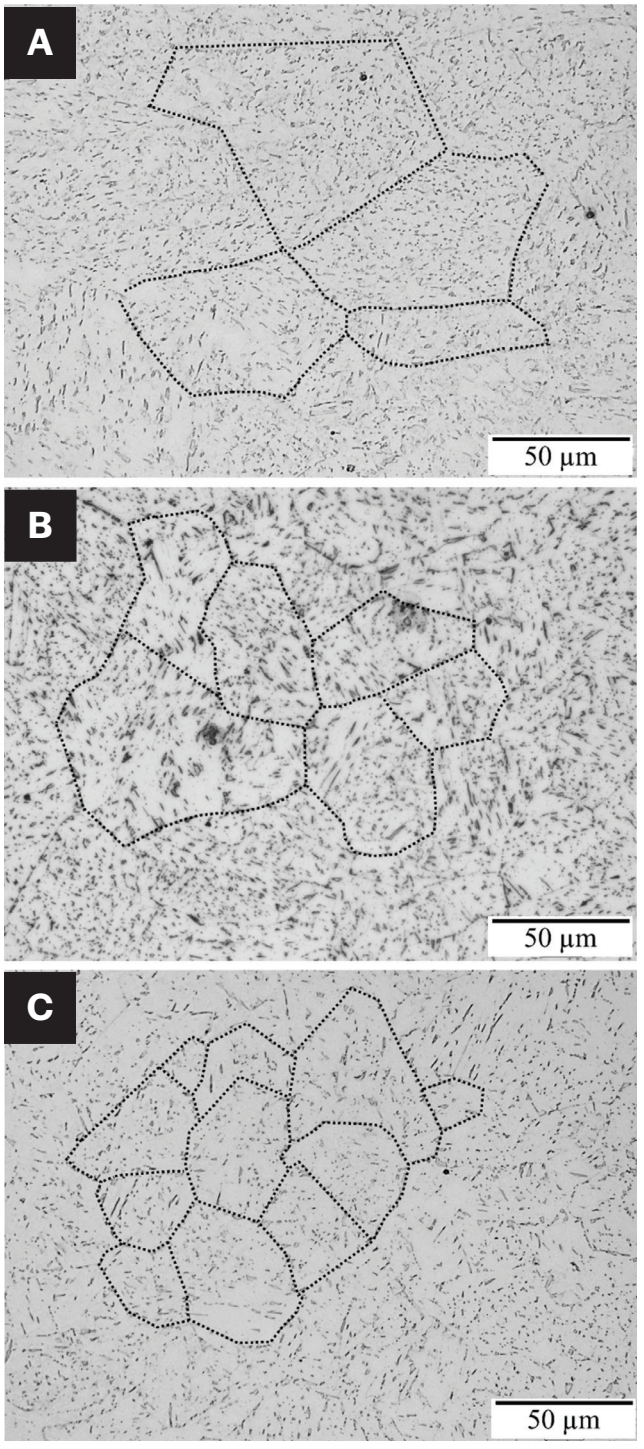

Fig. 4 — Optical micrographs of the CGHAZ: A — 2.9 kJ/mm; B — 2.6 kJ/mm; C — 2.3 kJ/mm. Prior austenite grain (PAG) boundaries are shown with dotted lines.

$$HI_{Nominal}\left(\frac{kJ}{mm}\right) = \frac{\mu}{1000 \cdot TS} \cdot [(V \cdot I)_{Lead} + (V \cdot I)_{Trail}] \quad (1)$$

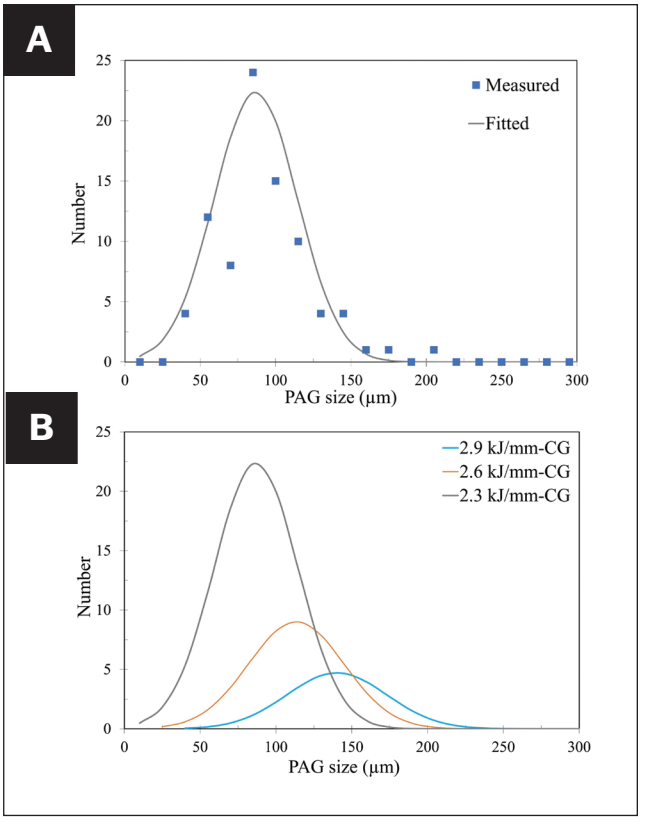

Fig. 5 — A — Measured and fitted normal distribution of PAG size in the CGHAZ of 2.3 kJ/mm; B — fitted normal distributions for all welds.

where µ represents the arc efficiency for SAW, which ranges from 0.9–1.0. Three test welds were made using three levels of CWFR, including 0 mm/s, 16.9 mm/s, and 33.9 mm/s. A previous study reported calculations of the effective heat input for each weld, which are listed in Table 2 (Ref. 19). To maintain consistency, the three welds were labeled as 2.9 kJ/mm, 2.6 kJ/mm, and 2.3 kJ/mm. The effective heat input calculation consists of the enthalpy change for cold wire fusion and the effect of arc instability on $HI_{Nominal}$, which are correlated with the PAG size and MA morphology results in the "Discussion" section.

Metallographic Sample Preparation

All weldments were inspected visually to confirm weld quality. Following visual inspection, metallographic samples were extracted from three locations along the weld and were labeled as 1, 2, and 3 (Fig. 2). In total, nine specimens (3 welds × 3 specimens) were mounted and polished according to ASTM E3-11, *Standard Guide for Preparation of Metallographic Specimens* (Ref. 20). The sample surfaces were polished to a 0.05 µm finish and etched. Nital (2%) was used to reveal the overall microstructure, modified LePera (LePera etchant with a few drops of HCl) revealed MA regions, and modified Picral solution (4 g picric acid in 96 ml distilled water with a few drops of HCl) was utilized to reveal the PAG boundaries (Ref. 19).

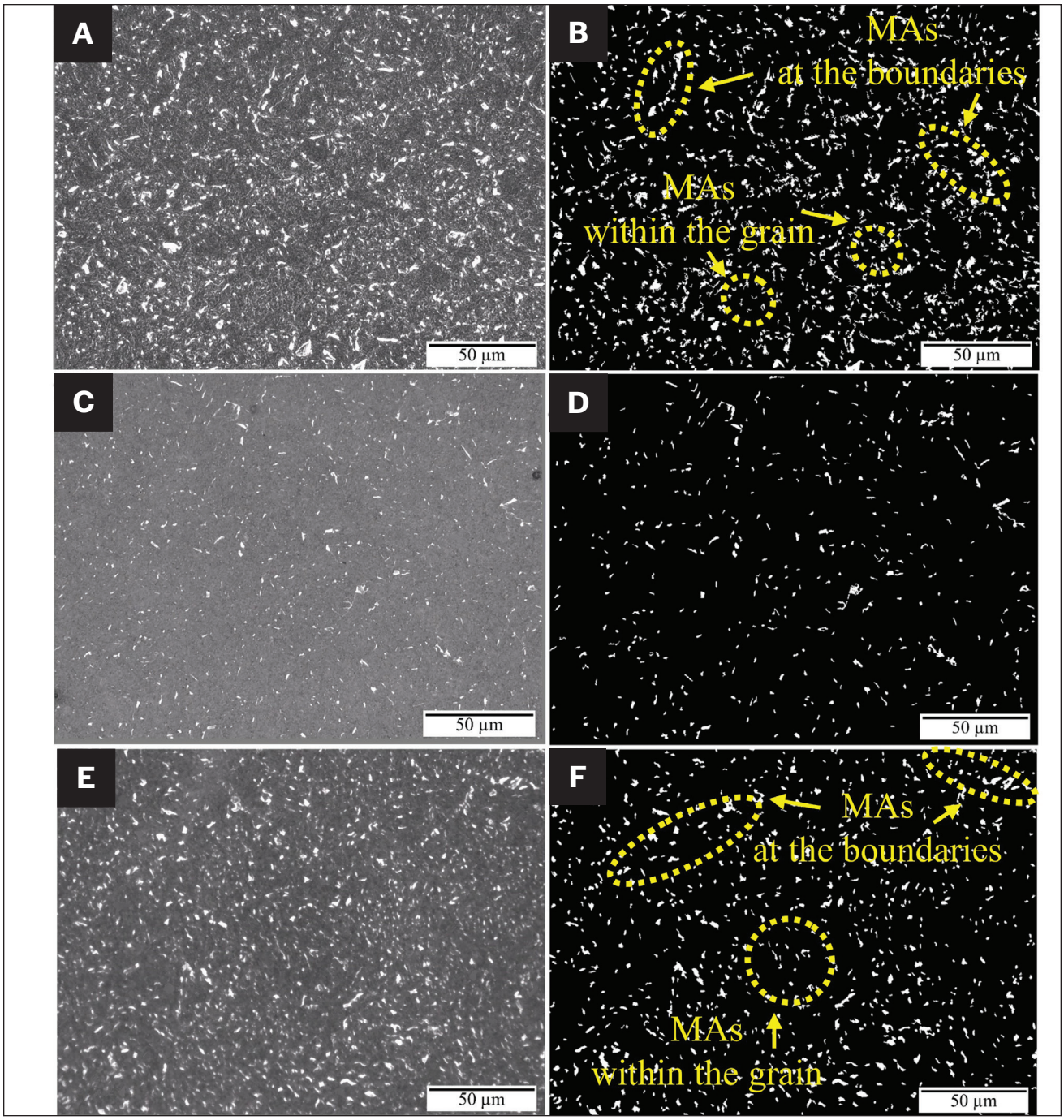

Fig. 6 — Optical (A, C, E) and processed (B, D, F) micrographs of martensite-austenite (MA) constituents in the CGHAZ: A, B — 2.9 kJ/mm; C, D — 2.6 kJ/mm; E, F — 2.3 kJ/mm. MA constituents at PAG boundaries and within PAG grains are indicated with yellow dashed circles and arrows, respectively.

Microstructural Characterization

Optical microscopy was undertaken using an Olympus BX61 microscope. SEM analysis of each sample was conducted using a Zeiss EVO M10 SEM operating at 20 kV accelerating voltage. OM micrographs were taken from both sides of the weld at a location 4 mm below the weld surface and 50–200 µm from the fusion line (in the CGHAZ). OM micrographs were also taken 600–800 µm from the fusion line in the FGHAZ. OM micrographs were processed by imaging software (MATLAB R2022b and ImageJ) to quantify PAG size in the CGHAZ and the morphology (aspect ratio and area) of each MA constituent in both the CGHAZ and FGHAZ (Ref. 19). SEM analysis was used to confirm the MA morphology observed in OM micrographs.

Results

Microstructure in CGHAZ and FGHAZ

Figures 3A, C, and E are OM micrographs (Nital etched) of the CGHAZ for the 2.9 kJ/mm, 2.6 kJ/mm, and 2.3 kJ/mm samples, respectively. Fig. 3A (2.9 kJ/mm) includes a portion of the weld metal in the upper left corner, as delineated by the dashed line. The microstructures of the 2.6 kJ/mm and 2.3 kJ/mm samples in the CGHAZ were similar and consisted primarily of bainite and a small amount of ferrite. The microstructure of the 2.9 kJ/mm sample was composed of similar phases, although the bainite laths were qualitatively coarser. Figures 3B, D, and F are OM micrographs of the FGHAZ for the 2.9 kJ/mm, 2.6 kJ/mm, and 2.3 kJ/mm samples, respectively. The FGHAZ microstructures for the 2.9 kJ/mm, 2.6 kJ/mm, and 2.3 kJ/mm samples were all similar and consisted of primarily polygonal ferrite and a small amount of bainite.

Prior Austenite Grain (PAG) Size Distribution

Optical micrographs (Picral etched) of the CGHAZ for the 2.9 kJ/mm, 2.6 kJ/mm, and 2.3 kJ/mm samples are shown in Figs. 4A, B, and C, respectively. Each micrograph highlights selected PAG grains and boundaries with black dotted lines. Qualitatively, the PAG size was largest for the 2.9 kJ/mm sample and finest for the 2.3 kJ/mm sample.

The measured PAG size (from a 0.5 mm^2 area) of the CGHAZ and the fitted normal distribution curve for the 2.3 kJ/mm (CGHAZ) sample are shown in Fig. 5A. The mean PAG size for 2.3 kJ/mm-CG was 86.8 µm. The maximum measured grain size was 198.3 µm. Figure 5B compares all of the welds' PAG size distributions for the CGHAZ. The 2.3 kJ/mm sample had the finest PAG size, while the 2.9 kJ/mm sample had the largest overall PAG size. The mean PAG sizes for the 2.9 kJ/mm and 2.6 kJ/mm samples were 140 and 113 µm, respectively. The differences observed in the mean PAG size and PAG distribution are attributed to differences in the effective heat input for each weld (Table 2) due to the introduction of the cold wire. The higher effective heat input for the 2.9 kJ/mm sample resulted in a larger PAG grain size.

MA Characterization

OM micrographs (LePera etched) of the CGHAZ of the 2.9 kJ/mm, 2.6 kJ/mm, and 2.3 kJ/mm samples are shown in Figs. 6A, C, and E, respectively. In each image, the MA constituent appears as white features after etching. The white features were confirmed as MA in a previous study using selected area electron diffraction in transmission electron microscopy analysis (Ref. 9). Figures 6B, D, and F are processed micrographs from Figs. 6A, C, and E that were used to analyze the MA morphology. Two types of MA distributions—MA constituents at PAG boundaries and MA within PAGs—were observed and are indicated with dashed yellow circles in Figs. 6B and 6F. This observation is discussed in the "Overlapping Log-Normal Distributions of MA Morphology" section. Qualitatively, the 2.9 kJ/mm and 2.3 kJ/mm samples showed significantly larger MA constituents than the 2.6 kJ/mm samples.

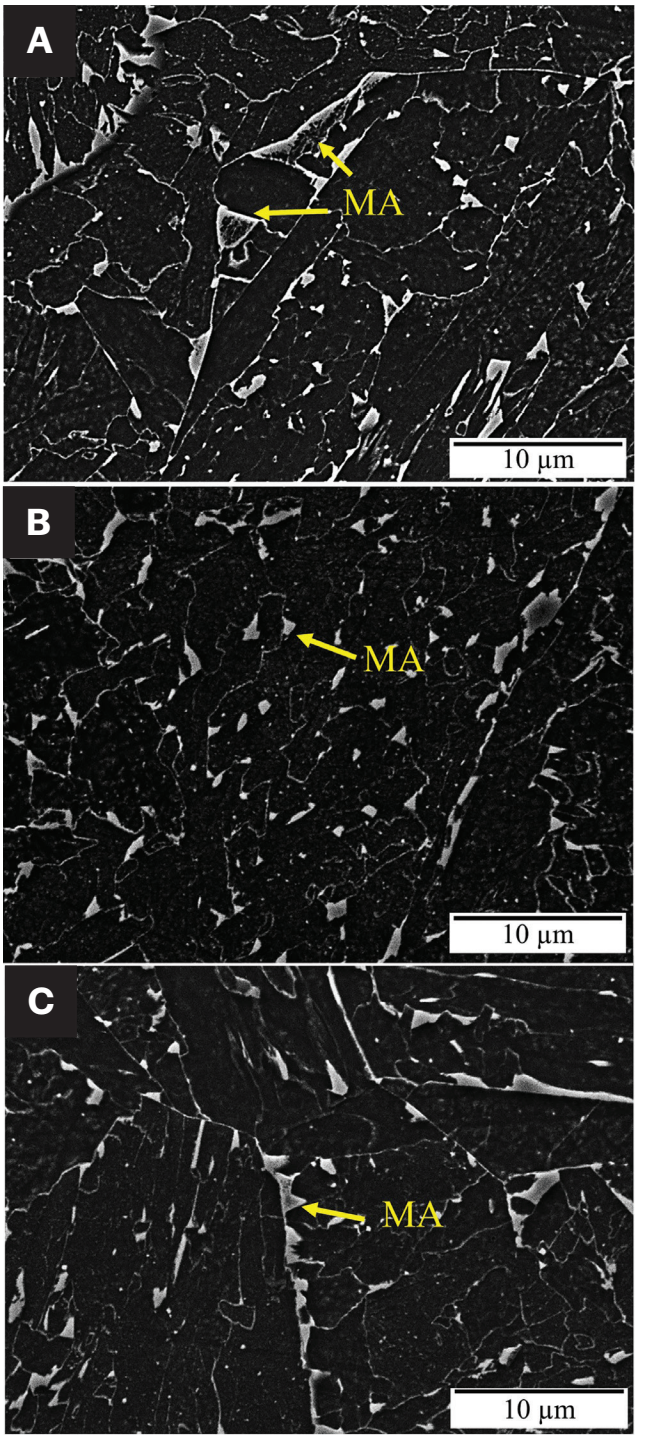

Fig. 7 — SEM secondary electron (SE) micrographs of MA constituents in the CGHAZ: A — 2.9 kJ/mm; B — 2.6 kJ/mm; C — 2.3 kJ/mm.

Figures 7A–C are higher magnification SEM images of select CGHAZ regions from Figs. 6A, C, and E for the 2.9 kJ/mm, 2.6 kJ/mm, and 2.3 kJ/mm samples, respectively. The observed necklace shape and massive MA constituents for the 2.9 kJ/mm and 2.3 kJ/mm samples (Figs. 6A and

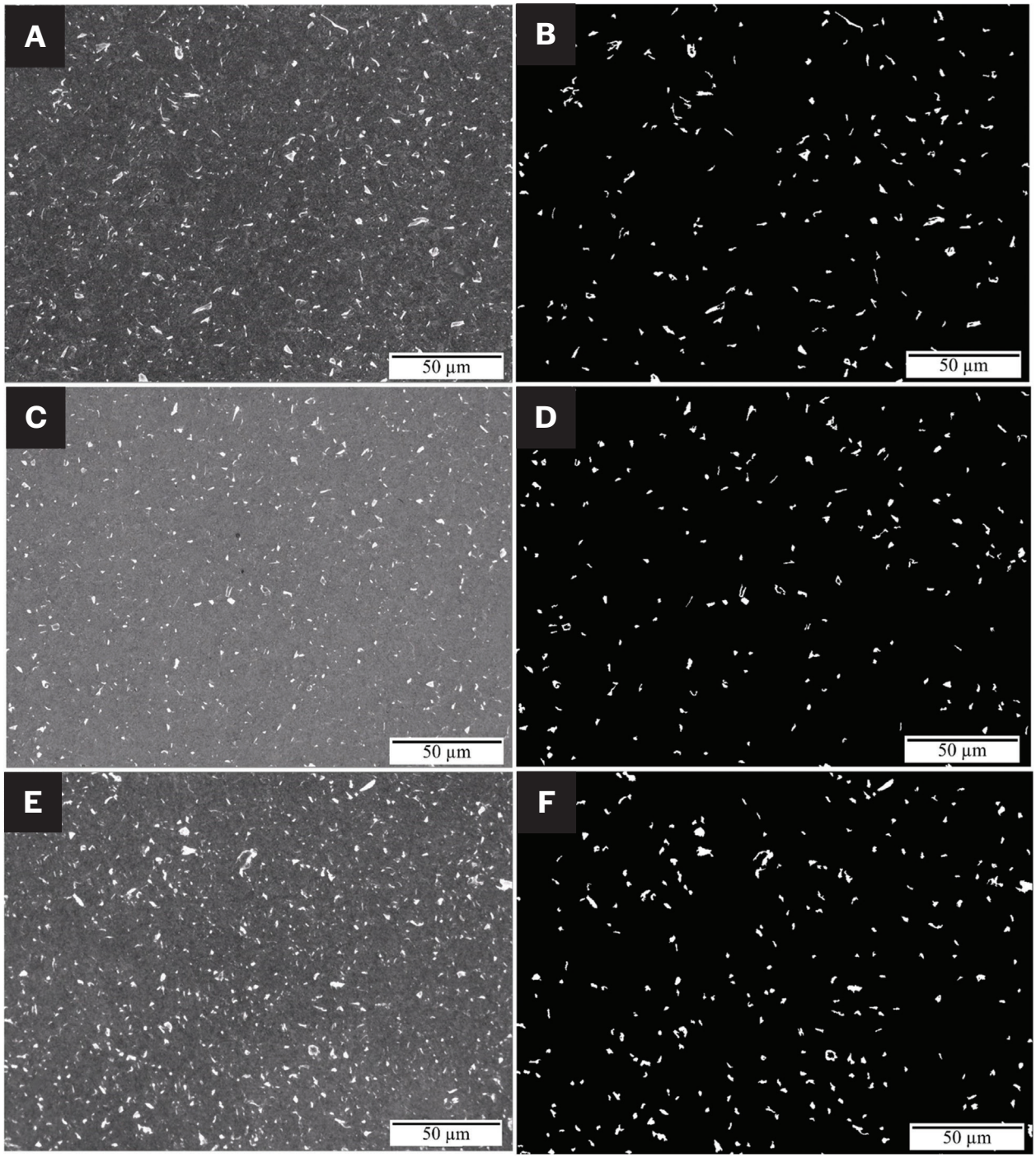

Fig. 8 — Optical (A, C, E) and processed (B, D, F) micrographs of MA constituents in the FGHAZ: A, B — 2.9 kJ/mm; C, D — 2.6 kJ/mm; E, F — 2.3 kJ/mm.

E) and finer size MA for 2.6 kJ/mm samples (Fig. 6C) were confirmed by SEM micrographs.

OM micrographs from the FGHAZ of the 2.9 kJ/mm, 2.6 kJ/mm, and 2.3 kJ/mm samples are shown in Figs. 8A, C and 8E, respectively. Figs. 8B, D, and 8F are micrographs processed with ImageJ, which was used to analyze MA morphology. Qualitatively, the FGHAZ of the 2.9 kJ/mm and 2.3 kJ/mm samples showed a lower amount and smaller size of MA constituents than in the CGHAZ (Figs. 6A and E). Alternatively, the FGHAZ of the 2.6 kJ/mm sample had slightly more MA with a similar size compared with the CGHAZ of the same sample (Fig. 6C).

Morphology of MA

The MA constituent area and aspect ratios in the CGHAZ and FGHAZ were measured from the OM micrographs shown in

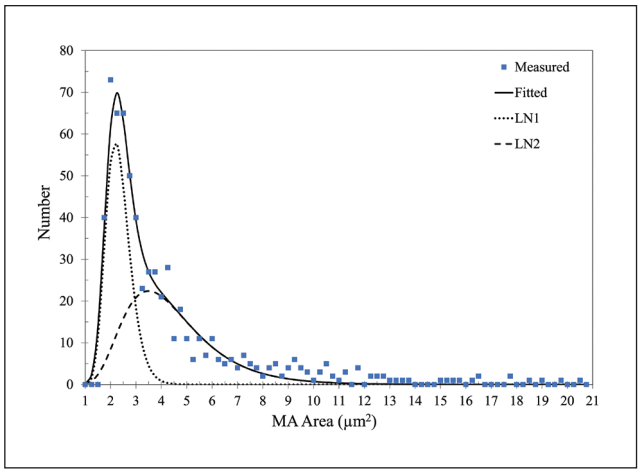

Fig. 9 — Measured and fitted log-normal distributions of the MA area for the CGHAZ for the 2.9 kJ/mm sample.

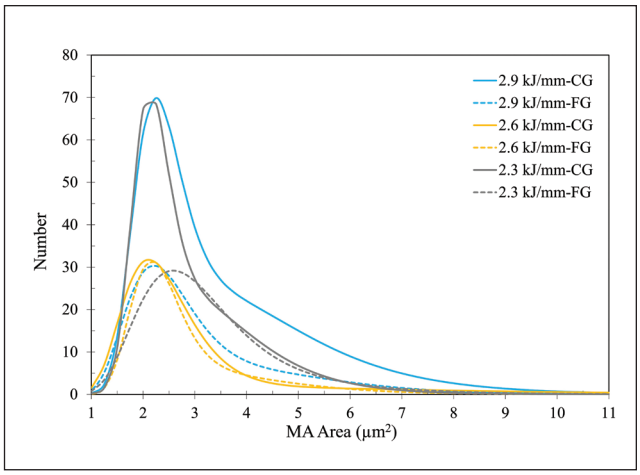

Fig. 10 — Fitted log-normal distributions of the MA area for all welds in the CGHAZ and FGHAZ.

Table 3 — Summation of MA Area Measurements and P-Values from the Kolmogorov-Smirnov (K-S) Test in Both the CGHAZ and FGHAZ for All Weld Samples

	2.9 kJ/mm		2.6 kJ/mm		2.3 kJ/mm	
	CGHAZ	FGHAZ	CGHAZ	FGHAZ	CGHAZ	FGHAZ
Total Number	648	197	162	174	443	260
Maximum Size (μm²)	32.3	18.2	15.6	9.8	20.7	23.9
Number > 5 μm²	148	37	21	26	91	44
Mean Area (μm²)	4.3 (0.2)	3.8 (0.2)	3.2 (0.2)	3.3 (0.1)	3.8 (0.1)	3.9 (0.2)
Mean Area MA in LN1	2.3	2.5	2.4	2.3	2.2	2.0
Mean Area MA in LN2	4.4	5.2	7.4	4.2	3.5	5.2
Number Ratio LN1/LN2	0.80	3.5	5.2	2.6	0.83	14
Total Area Fraction (%)	7.0	1.87	1.30	1.43	4.19	2.53
P-Value of K-S Test for LN1	0.66	0.67	0.70	0.62	0.71	0.51
P-Value of K-S Test for LN2	0.47	0.17	0.36	0.45	0.50	0.25

Note: LN1 refers to log-normal distribution 1 and LN2 refers to log-normal distribution 2. The values in the brackets are one standard deviation. K-S test refers to the Kolmogorov-Smirnov test and P values greater than 0.05 indicating an accepted goodness of fit of the log-normal distributions at 5% confidence level.

Figs. 6 and 8, respectively. All MA constituents less than three (3) pixels in size (3.82 pixels/μm) were not included in the count number. The measured and fitted (log-normal) MA area distributions in the CGHAZ (2.9 kJ/mm-CG) for the 2.9 kJ/mm sample are shown in Fig. 9. The fitted log-normal distribution (solid line) is composed of two overlapping log normal distributions: LN1 (dotted line) and LN2 (dash line). The mean values of the MA area in the CGHAZ of the 2.9 kJ/mm samples for LN1 and LN2 were 2.3 μm² and 4.1 μm², respectively. The ratio of MA constituents in each area distribution (LN1/LN2) was 0.80, indicating more MA in the larger MA area distribution LN2 than in the finer MA area distribution LN1. The significance of the

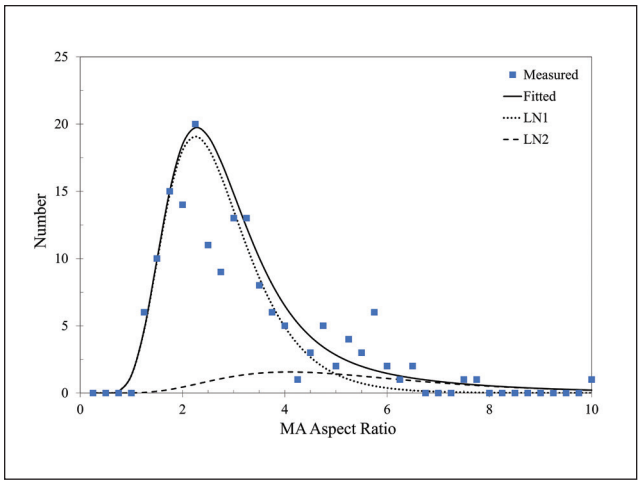

Fig. 11 — Measured and fitted log-normal distributions of the aspect ratio (AR) for the 2.6 kJ/mm sample in the CGHAZ.

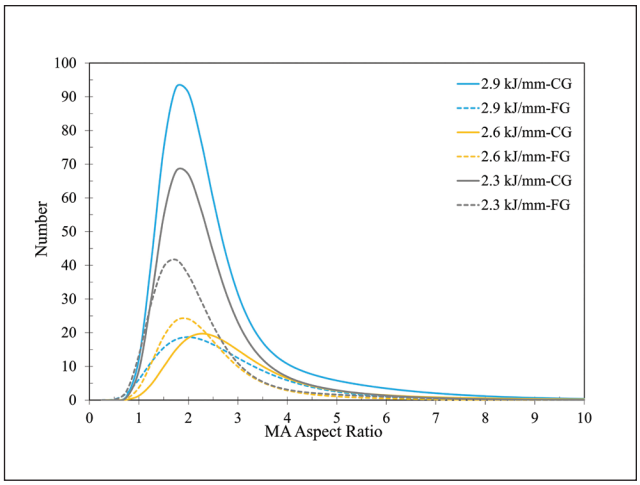

Fig. 12 — Fitted log-normal distributions of the AR for all welds in the CGHAZ and FGHAZ.

Table 4 — Summation of MA Aspect Ratio Measurements and P-Values from the Kolmogorov-Smirnov (K-S) Test in Both the CGHAZ and FGHAZ for All Weld Samples

	2.9 kJ/mm		2.6 kJ/mm		2.3 kJ/mm	
	CGHAZ	FGHAZ	CGHAZ	FGHAZ	CGHAZ	FGHAZ
Maximum AR	6.8	9.7	10.0	6.9	8.9	6.5
Number of AR > 4	36	24	32	13	34	10
Mean AR	2.2 (0.1)	2.7 (0.1)	3.0 (0.1)	2.4 (0.1)	2.3 (0.1)	2.1 (0.1)
Mean AR in LN1	2.1	2.5	2.5	2.1	2.0	1.9
Mean AR in LN2	4.0	—	5.0	4.5	3.5	5.0
Number ratio LN1/LN2	3.7	—	5.0	13.5	2.7	13.0
P-Value of K-S Test for LN1	0.66	0.67	0.68	0.65	0.66	0.79
P-Value of K-S Test for LN2	0.40	—	0.06	0.053	0.58	0.051

Note: LN1 refers to log-normal distribution 1 and LN2 refers to log-normal distribution 2. The values in the brackets are one standard deviation. K-S test refers to the Kolmogorov-Smirnov test and P-values greater than 0.05 indicating an accepted goodness of fit of the log-normal distributions at 5% confidence level.

MA area exhibiting two overlapping log-normal distributions will be discussed later. The maximum measured MA area for 2.9 kJ/mm-CG was 32.3 μm². The number of MA constituents with an area > 5 μm² was 148, the area fraction (Fig. 6A) was 7.0%, and the total number of distinct MA constituents in an area of 0.04 μm² (Fig. 6A) was 648.

Figure 10 compares the MA area in the CGHAZ (CG) and the FGHAZ (FG) for all the weld samples. The MA areas in both the 2.9 kJ/mm-CG and 2.3 kJ/mm-CG samples had significantly more MA constituents than in the 2.6 kJ/mm-CG in the area range from ≈2 μm² to 3 μm². The MA area distributions for the 2.9 kJ/mm-FG, 2.6 kJ/mm-CG, 2.6 kJ/mm-FG, and

2.3 kJ/mm-FG were similar. Table 3 summarizes the MA area characteristics for all weld samples and P-values from the Kolmogorov-Smirnov (K-S) test. The goodness of fit of the log-normal distributions was assessed from the P-value and the confidence level of the K-S test (Ref. 21). Table 3 shows that all P-values for the MA areas in the LN1 and LN2 distributions were greater than 0.05, which indicates an acceptable goodness of fit of the log-normal distributions at a 5% confidence level. The CGHAZ regions for the 2.9 kJ/mm and 2.3 kJ/mm samples had the largest total number of MA constituents and the highest number of large ($> 5\ \mu m^2$) MA constituents. In addition, the number ratio (LN1/LN2) was less than 1.0 for both the 2.9 kJ/mm-CG and 2.3 kJ/mm-CG samples. This indicates that the number of MA constituents in the larger MA size distribution (LN2) was greater than the number of MA in the finer size distribution (LN1). For the FGHAZ and the CGHAZ of the 2.6 kJ/mm samples, the ratio of LN1/LN2 was greater than 1, indicating that most of the MA particles were in the fine size distribution (LN1).

The measured and fitted distributions of the MA aspect ratio in the CGHAZ for the 2.6 kJ/mm sample are shown in Fig. 11. The fitted log-normal distribution (solid line) is composed of two overlapping log normal distributions: LN1 (dotted line) and LN2 (dashed line). The mean values of aspect ratio for LN1 and LN2 were 2.9 and 5.2, respectively. The maximum measured aspect ratio for the 2.6 kJ/mm-CG sample was 10, and the number of MA constituents with aspect ratio > 4 was 32.

Figure 12 compares the aspect ratio distribution for all welds in the CGHAZ and the FGHAZ. Most of the MA constituents in the CGHAZ for all samples had an aspect ratio ranging from ≈1 to 3, with a peak near 2.

Table 4 summarizes aspect ratio characteristics and P-values from the K-S test for all weld samples. The goodness of fit values for the log-normal distributions for the MA aspect ratio LN1 and LN2 distributions were acceptable. The CGHAZ for the 2.9 kJ/mm sample had the greatest number of MA constituents with an aspect ratio > 4.

Discussion

Overlapping Log-Normal Distributions of MA Morphology

Tables 3 and 4 show that the MA areas and aspect ratios followed two overlapping log-normal distributions. The presence of two distributions (one exhibiting a lower mean size and one exhibiting a larger mean size) was observed primarily in the CGHAZ and, to a lesser extent, in the FGHAZ. The two distributions suggested that MA constituents in the CGHAZ were formed at the PAG boundaries and bainite lath boundaries. Figures 6B and F (the CGHAZ in the 2.9 kJ/mm and 2.3 kJ/mm samples) qualitatively exhibit coarse stringer MA constituents in the vicinity of the PAG boundaries and a finer MA morphology within the interior of the grains (along lath boundaries of the bainitic microstructure). In particular, the coarse stringer MA constituents along the PAG boundaries appear to be correlated with PAG size as the 2.3 kJ/mm weld had a finer PAG size than the 2.6 kJ/mm weld, so there were more PAG boundaries with more sites for the formation of coarse MA constituents in the 2.3 kJ/mm sample. The variation in MA morphology and PAG size, correlated with the effective heat input, will be discussed in the following section.

Effect of Heat Input on MA Morphology and PAG Size

The number, areas, and aspect ratios of MA constituents were higher for the 2.9 kJ/mm (highest heat input) and 2.3 kJ/mm samples (lowest heat input) relative to the 2.6 kJ/mm sample (Figs. 6 and 8 and Tables 3 and 4). The 2.6 kJ/mm sample (smallest number, area, and aspect ratio of MA) had an intermediate effective heat input (2.6 kJ/mm). The 2.9 kJ/mm sample, with the highest heat input, had the largest PAG size, which can be attributed to the amount/width of material experiencing significant time at or above grain coarsening temperatures (e.g., a temperature sufficient to dissolve Nb (C.N) precipitates [Ref. 1] in the CGHAZ). The large PAG size in the 2.9 kJ/mm meant fewer nucleation sites for ferrite formation, which increased the probability of MA formation. Coarser PAGs and larger MA constituents result in reduced toughness (Refs. 5, 14). The 2.3 kJ/mm sample, with the lowest heat input and smallest PAG size, might be expected to form less MA. However, the faster cooling rate associated with the low heat input promotes martensite formation, resulting in a high MA area fraction with large MA constituents (Ref. 22).

Conclusions

The effects of cold wire feed rate on martensite-austenite constituent morphology and prior austenite grain size of cold-wire tandem submerged-arc welded X70 steel were studied. The main conclusions are as follows:

1. The number and, to a lesser extent, size (aspect ratio and area) of MA was higher in the CGHAZ for welds without cold wire addition (effective heat input of 2.9 kJ/mm) and for the fastest CWFR of 33.9 mm/s (effective heat input of 2.3 kJ/mm).

2. An intermediate CWFR of 16.9 mm/s (effective heat input of 2.6 kJ/mm) resulted in fewer and smaller MA regions in the CGHAZ.

3. PAG size decreased as the effective heat input decreased due to less duration above A_{C1}. Both coarse PAGs (fewer nucleation sites for ferrite formation) and fast cooling rates resulted in the formation of coarse MA within the CGHAZ of samples with the highest and lowest effective heat input, respectively.

4. For all welds, the number and size of MA constituents in the FGHAZ were less affected by the effective heat input than the MA constituents in the CGHAZ.

5. A balance between the duration above A_{c1} and the cooling rate in the CGHAZ of heavy gauge X70 steel can minimize the number of coarse MA constituents in the CGHAZ.

In Part 2 of this two-part article, the quantitative effect of MA morphology and PAG size distribution on the fracture toughness (Charpy impact energies, energy values, crack path, and notch placement) will be studied and discussed.

Acknowledgments

The authors would like to acknowledge the Natural Sciences and Engineering Research Council (NSERC) of Canada, Evraz Inc. NA, and TC Energy Corp. for providing financial support. The assistance of Mohsen Mohammadijoo with welding trials is appreciated. The R&D Division of Evraz Inc. NA is recognized for providing welding equipment and technical assistance in conducting welding trials and CVN testing.

References

1. Collins, L., Dunnett, K., Hylton, T., and Ray, A. 2018. Development of heavy gauge X70 helical line pipe. *ASME - International Pipeline Conference*. DOI: 10.1115/IPC2018-78763

2. Ren, T., Mohammadijoo, M., Wiskel, J. B., Lazor, R., Willett, E., Ivey, D. G., and Henein, H. 2022. Effect of cold wire addition in tandem submerged arc welding on weld geometry and micro-hardness of heavy gauge X70 steel. *The International Journal of Advanced Manufacturing Technology* 121(11–12): 7607–7625. DOI: 10.1007/s00170-022-09698-9

3. Concurrent Technologies Corp. 2006. Cold wire feed submerged arc welding. Retrieved from *nsrp.org/wp-content/uploads/2015/09/Deliverable-2006-354-Cold_Wire_Feed_SAW_Final_Report-Concurrent_Technologies_Corporation.pdf.*

4. Mohammadijoo, M., Collins, L., Lazor, R., Henein, H., and Ivey, D. G. 2018. Influence of cold-wire submerged arc welding on the toughness of microalloyed steel. *Welding Journal* 97(12): 338-s to 352-s. DOI: 10.29391/2018.97.029

5. Mohammadijoo, M., Kenny, S., Collins, L., Henein, H., and Ivey, D. G. 2017. Characterization of HAZ of API X70 microalloyed steel welded by cold-wire tandem submerged arc welding. *Metallurgical and Materials Transactions A: Physical Metallurgy and Materials Science* 48(5): 2247–2259. DOI: 10.1007/s11661-017-4041-x

6. Xie, C., Liu, Z., He, X., Wang, X., and Qiao, S. 2020. Effect of martensite–austenite constituents on impact toughness of pre-tempered MnNiMo bainitic steel. *Materials Characterization* 161(3): 110139. DOI: 10.1016/j.matchar.2020.110139

7. Ramachandran, D. C., Kim, S.-D., Moon, J., Lee, C.-H., Chung, J. H., Biro, E., and Park, Y.-D. 2020. Classification of martensite-austenite constituents according to its internal morphology in high-strength low alloy steel. *Materials Letters* 278: 128422. DOI: 10.1016/j.matlet.2020.128422

8. Yang, X., Di, X., Liu, X., Wang, D., and Li, C. 2019. Effects of heat input on microstructure and fracture toughness of simulated coarse-grained heat affected zone for HSLA steels. *Materials Characterization* 155(9). DOI: 10.1016/j.matchar.2019.109818

9. Mohammadijoo, M., Valloton, J., Collins, L., Henein, H., and Ivey, D. G. 2018. Characterization of martensite-austenite constituents and micro-hardness in intercritical reheated and coarse-grained heat affected zones of API X70 HSLA steel. *Materials Characterization* 142(8): 321–331. DOI: 10.1016/j.matchar.2018.05.057

10. Reichert, J. M., Poole, W. J., Militzer, M., and Collins, L. 2014. A new approach using EBSD to quantitatively distinguish complex transformation products along the HAZ in X80 linepipe steel. *International Pipeline Conference*. DOI: doi.org/10.1115/IPC2014-33668

11. Zhu, Z., Kuzmikova, L., Li, H., and Barbaro, F. 2014. Effect of inter-critically reheating temperature on microstructure and properties of simulated inter-critically reheated coarse grained heat affected zone in X70 steel. *Materials Science and Engineering A* 605: 8–13. DOI: 10.1016/j.msea.2014.03.034

12. Di, X. J., An, X., Cheng, F. J., Wang, D. P., Guo, X. J., and Xue, Z. K. 2016. Effect of martensite–austenite constituent on toughness of simulated inter-critically reheated coarse-grained heat-affected zone in X70 pipeline steel. *Science and Technology of Welding and Joining* 21(5): 366–373. DOI: 10.1080/13621718.2015.1118814

13. Li, C., Wang, Y., and Chen, Y. 2011. Influence of peak temperature during in-service welding of API X70 pipeline steels on microstructure and fracture energy of the reheated coarse grain heat-affected zones. *Journal of Materials Science* 46(19): 6424–6431. DOI: 10.1007/s10853-011-5592-7

14. Huda, N., Wang, Y., Li, L., and Gerlich, A. P. 2019. Effect of martensite-austenite (MA) distribution on mechanical properties of inter-critical reheated coarse grain heat affected zone in X80 linepipe steel. *Materials Science and Engineering A* 765(9): 138301. DOI: 10.1016/j.msea.2019.138301

15. Li, X., Ma, X., Subramanian, S. V., Shang, C., and Misra, R. D. K. 2014. Influence of prior austenite grain size on martensite-austenite constituent and toughness in the heat affected zone of 700MPa high strength linepipe steel. *Materials Science and Engineering A* 616: 141–147. DOI: 10.1016/j.msea.2014.07.100

16. AWS D1.7/D1.7M. 2010, *Guide for strengthening and repairing existing structures*. Miami, Fla.: American Welding Society.

17. AWS A5.23/A5.23M. 2021, *Specification for low-alloy and high manganese steel electrodes and fluxes for submerged arc welding*. Miami, Fla.: American Welding Society.

18. Pepin, J., Penniston, C., Henein, H., Ivey, D. G., Collins, L., and Boyd, D. 2012. Using semipenetration ratio to characterize effects of waveform variables on bead profile and heat affected zone with single electrode submerged arc welding. *Canadian Metallurgical Quarterly* 51(3): 284–293. DOI: 10.1179/1879139512Y.0000000018

19. Ren, T. 2021. Effect of cold wire TSAW on weld geometry and CGHAZ microstructure of heavy gauge X70. Master's thesis, University of Alberta. DOI: 10:7939/r3-qsjk-ej65

20. ASTM E3-11. 2017. *Standard guide for preparation of metallographic specimens*. ASTM International.

21. Olea, R. A., and Pawlowsky-Glahn, V. 2009. Kolmogorov-Smirnov test for spatially correlated data. *Stochastic Environmental Research and Risk Assessment* 23(6): 749–757. DOI: 10.1007/s00477-008-0255-1

22. Huda, N., Midawi, A. R. H., Gianetto, J., Lazor, R., and Gerlich, A. P. 2016. Influence of martensite-austenite (MA) on impact toughness of X80 line pipe steels. *Materials Science and Engineering A* 662: 481–491. DOI: 10.1016/j.msea.2016.03.095

TAILIN REN (*tailin@ualberta.ca*), **J. BARRY WISKEL**, **DOUGLAS G. IVEY**, **LEIJUN LI**, and **HANI HENEIN** are with the Department of Chemical and Materials Engineering, University of Alberta, Edmonton, Alberta, Canada. **LAURIE COLLINS** is with (formerly) R&D Division, EVRAZ Inc., Regina, Saskatchewan, Canada. **GREG LEHNHOFF** and **MICHAEL GAUDET** are with the R&D Division, EVRAZ Inc. NA, Regina, Saskatchewan, Canada. **ERIC WILLETT** is with TC Energy Corp., Calgary, Alberta, Canada.